INTERNATIONAL JOURNAL FOR NUMERICAL METHODS IN FLUIDS
Int. J. Numer. Meth. Fluids 2006; **50**:1297–1319
Published online 15 November 2005 in Wiley InterScience (www.interscience.wiley.com). DOI: 10.1002/fld.1121

Spectral element benchmark simulations of natural convection in two-dimensional cavities¶

Thor Gjesdal*,†, Carl Erik Wasberg‡ and Bjørn Anders Pettersson Reif§

Norwegian Defence Research Establishment, Kjeller, Norway

SUMMARY

This paper reports the results of spectral element simulations of natural convection in two-dimensional cavities. In particular, a detailed comparison is performed with the reference data for the 8:1 cavity at $Ra = 3.4 \times 10^5$ recently described by Christon *et al.* [*Int. J. Numer. Methods Fluids* 2002; **40**:953–980]. The Navier–Stokes equations augmented by the Boussinesq approximation to represent buoyancy effects are solved by a numerical method based on a spectral element discretization and operator splitting. The computed solutions agree closely with the reference data for both the square and the rectangular cavity configurations. Copyright © 2005 John Wiley & Sons, Ltd.

KEY WORDS: natural convection; 8:1 thermally driven cavity; incompressible flow; Boussinesq approximation; spectral element method; operator splitting

1. INTRODUCTION

We perform spectral element simulations of two-dimensional cavity where the flow is driven by the natural convection set up by differentially heated walls. The thermal cavity flow is an important prototype flow for a wide range of practical technological problems, including ventilation, crystal growth in liquids, nuclear reactor safety, and the design of high-powered laser systems. Cavity flows are furthermore often used as test cases for code verification and validation because they are simple to set up and reliable reference solutions are readily available, both for steady state [1–3] and time-dependent flows [4, 5]. Although the flow configuration is two-dimensional, thermal cavity flows display a plethora of interesting fluid

*Correspondence to: T. Gjesdal, Norwegian Defence Research Establishment, FFI, P.O. Box 25, NO-2027 Kjeller, Norway.
†E-mail: Thor.Gjesdal@ffi.no
‡E-mail: Carl-Erik.Wasberg@ffi.no
§E-mail: Bjorn.Reif@ffi.no
¶A preliminary version of this paper was presented at CHT-04: An ICHMT International Symposium on Advances in Computational Heat Transfer, April 2004, G. de Vahl Davis and E. Leonardi (eds), CD-ROM Proceedings, ISBN 1-5670-174-2, Begell House, New York, 2004.

Received 21 January 2005
Revised 21 September 2005
Accepted 21 September 2005

dynamic phenomena and complex features such as impinging boundary layers, stratification, and an intricate temporal behaviour with increasing Rayleigh number. Since these effects depend strongly on the cavity aspect ratio, thermal boundary conditions and Prandtl number, this test case constitutes a severe challenge for numerical schemes.

Spectral element methods have over the years been applied to compute a broad range of flow configurations, including thermal convection problems such as the Rayleigh–Bénard instability [6, 7], and turbulent forced convection [8–10]. A comprehensive assessment of the performance of spectral element methods for a standard convection benchmark problem, such as the differentially heated cavity, has however not been reported to date. Minev *et al.* [11] describe a spectral element operator splitting algorithm for thermal problems with computational examples from the cavity problem. The present contribution differs in several aspects from the work presented in Reference [11], and we will discuss these differences, both with respect to methodology and application, below. Finally, we note that Gunes [12] recently used a spectral element method to derive basis functions (POD modes) to develop a low-order dynamical model for the flow in very tall buoyancy driven cavities.

The objective of this study is to assess the numerical accuracy of our code and the spectral element method in a well-documented case. To do so we consider both steady state and time-dependent flows in square and rectangular cavities. Firstly, we perform a thorough comparison of the computed solutions against the reported benchmark data for the classical steady-state square cavity [1–3] over a large range of Rayleigh numbers. As mentioned above, few spectral element solutions appear to have been reported for this case. Secondly, we consider the slightly supercritical time-dependent flow in a tall cavity with aspect ratio 8:1. This configuration was the subject on a recent workshop reported by Christon *et al.* [4] in which a total of 31 solutions were submitted for this problem. The numerical method we employ differ in two respects from those reported at the workshop.

- The spectral element discretization.
- A time integration method based on an operator splitting of the advection–diffusion equations for momentum and temperature.

As such, the present work supplements the results reported earlier and extends the data base of results for this particular benchmark case.

In addition to presenting a 'best' solution to demonstrate the accuracy of the method, we study the impact of computational parameters such as the computational grid, time-step, and numerical tolerance parameters on the quality of the computed solutions, as well as the effect of the spatial filtering procedure developed by Fischer and Mullen [13] to reduce aliasing errors.

2. NUMERICAL METHOD

The equations describing the Boussinesq approximation for the dynamics of a viscous, incompressible fluid affected by buoyancy forces are

$$\nabla \cdot \mathbf{u} = 0 \tag{1a}$$

$$\frac{\partial \mathbf{u}}{\partial t} + \mathbf{u} \cdot \nabla \mathbf{u} = -\nabla p + \nu \nabla^2 \mathbf{u} + \beta (T - T_{\text{ref}}) \mathbf{g} \tag{1b}$$

$$\frac{\partial T}{\partial t} + \mathbf{u} \cdot \nabla T = \alpha \nabla^2 T \tag{1c}$$

where $\mathbf{u} = (u, v)$ represents the velocity, p represents the pressure, and T represents the temperature. The kinematic viscosity is denoted by ν, the thermal diffusivity by α, the coefficient of thermal expansion by β, and the gravitational acceleration $\mathbf{g} = (0, -g)$. The Boussinesq approximation is valid provided that the density variations, $\rho(T)$, are small; in practice this means that only small temperature deviations from the mean temperature are admitted.

The relevant non-dimensional parameters that characterize the flow are:

- the Prandtl number; $Pr = \nu/\alpha$,
- the Reynolds number; $Re = UL/\nu$, and
- the Rayleigh number; $Ra = g\beta\Delta TL^3/\nu\alpha$.

In addition, we must take into account a parameter that describes the geometry of the rectangular enclosure

- the aspect ratio; $A = H/W$,

where H and W denote the height and the width of the box, respectively. Note that the free convection cases we consider below are completely determined by the Prandtl number, the Rayleigh number, and the aspect ratio.

The numerical method we develop below is largely an extension to the Boussinesq equations of the Navier–Stokes solvers described by Couzy [14] and Fischer [15]. Minev *et al.* [11] describe a spectral element method for thermal problems that, in many respects, is similar to ours. There are some notable differences though, both in the methodology and in the application to the cavity problem. Firstly, whereas Minev *et al.* use a Runge–Kutta method with a fixed time step to integrate the hyperbolic (advective) parts of the operator-split momentum and temperature equations, we use an adaptive second-order Runge–Kutta method that lets the sub-cycling ratio, i.e. the number of explicit (hyperbolic) time steps per implicit (parabolic) time step, evolve with the solution. Secondly, Minev *et al.* employ a continuous pressure correction method to enforce mass conservation. There are some accuracy issues with this approach, both with respect to the formulation of the pressure equation and boundary conditions, that are naturally avoided by employing the pressure correction and enforcing the incompressibility condition at the discretized level as we describe below.

2.1. Time discretization

The key to an efficient and accurate solution of the Boussinesq/Navier–Stokes system (1) is a judicious use of implicit–explicit splitting for terms of different character. In particular, if the advection–diffusion equations are solved by an implicit–explicit procedure, the temperature equation can be decoupled from the remaining momentum equations. The buoyancy source term can then be calculated first and fed directly to the Navier–Stokes solver. In addition to the diffusive terms, we also treat the pressure term and the divergence equation implicitly.

In the temporal discretization based on the implicit–explicit time splitting we treat the advection–diffusion equations for the temperature and the velocities according to the operator-integration-factor (OIF) method of Maday *et al.* [16]. The advective terms are integrated explicitly by an adaptive second-order accurate Runge–Kutta method, while the viscous terms

are integrated by the implicit second-order backward difference scheme (BDF2), given by

$$\frac{\partial u}{\partial t} = \frac{3u^{n+1} - 4u^n + u^{n-1}}{2\Delta t} + O(\Delta t^2)$$

After discretization in time we can write (1) in the form

$$\frac{3T^{n+1} - 4T^n + T^{n-1}}{2\Delta t} - \alpha \nabla^2 T^{n+1} = -(\mathbf{u} \cdot \nabla T)^* \tag{2a}$$

$$\frac{3\mathbf{u}^{n+1} - 4\mathbf{u}^n + \mathbf{u}^{n-1}}{2\Delta t} - \nu \nabla^2 \mathbf{u}^{n+1} = -\nabla p^{n+1} - (\mathbf{u} \cdot \nabla \mathbf{u})^* + \beta(T^{n+1} - T_{\text{ref}})\mathbf{g} \tag{2b}$$

$$\nabla \cdot \mathbf{u}^{n+1} = 0 \tag{2c}$$

where the terms $(\mathbf{u} \cdot \nabla T)^*$ and $(\mathbf{u} \cdot \nabla \mathbf{u})^*$ are at least second-order accurate explicit approximations of the advection terms for temperature and velocity, respectively. The resulting scheme is thus second-order accurate in time. Note that we have changed the ordering of the equations in (2) to emphasize that the temperature at the new time level, T^{n+1}, can be obtained from known velocity data.

2.2. Space discretization

The spatial discretization is based on a spectral element method [17, 18]; the computational domain is sub-divided into non-overlapping quadrilateral (in 2D) or hexahedral (in 3D) cells or elements. Within each element, a weak representation of (2) is discretized by a Galerkin method in which we choose the test and trial functions from bases of polynomial spaces, i.e.

$$u_i^h \in P_N(x) \otimes P_N(y) \otimes P_N(z) \tag{3a}$$

$$p^h \in P_{N-2}(x) \otimes P_{N-2}(y) \otimes P_{N-2}(z) \tag{3b}$$

where $P_N(x)$ denotes the function space spanned by polynomials of degree N. Note that we employ a lower-order basis for the pressure spaces to avoid spurious pressure modes in the solution [18]. The velocity variables are C^0-continuous across element boundaries and they are represented at the Gauss–Lobatto–Legendre (GLL) points for the numerical integration, whereas the pressure variable is discontinuous across element boundaries and are represented at the interior Gauss–Legendre (GL) points. The one-dimensional polynomial basis functions, $h_j(\xi)$, are defined as the Lagrange interpolants that vanish at all but one of the GLL and GL points, respectively, such that

$$h_j(\xi_i) = \delta_{ij} \tag{4}$$

where ξ_i represents the GLL or GL grid point positions.

2.3. Polynomial filtering

The GLL grid corresponding to the Legendre polynomial of degree N has $(N+1)$ points. GLL quadrature at the $(N+1)$ GLL points is exact for polynomial of degree $(2N-1)$. Hence, the computation of the inner products corresponding to the diffusive terms in (1) are calculated exactly, whereas the evaluation of the non-linear advective terms incurs quadrature (aliasing)

errors. These errors can be detrimental to the stability of the method and must be controlled. The most fundamental approach to de-aliasing is to perform over-integration [19, 20]—that is, to over-sample and to use more quadrature points to evaluate the inner products containing non-linear terms. A computationally more efficient alternative approach is to use polynomial filtering of the solutions as proposed by Fischer and Mullen [13]. The filtering comprises a weighted sum of the original unfiltered field, u_N, and its projection onto the space of polynomials of degree $(N-1)$. If I_n^m is the interpolation operator from the n-point to the m-point GLL grid, the one-dimensional projection operator can be written $\Pi_{N-1} = I_{N-1}^N I_N^{N-1}$, and the filter is defined by

$$F_\eta \equiv \eta \Pi_{N-1} + (1-\eta) I \tag{5}$$

where η is a filter parameter. Filter functions in two and three dimensions are constructed by tensor products of the one-dimensional filter.

2.4. Solution of the discretized equations

For the solution of the discretized Boussinesq/Navier–Stokes system (1), we introduce the discrete Helmholtz operator,

$$H_\varepsilon = \kappa B + \varepsilon A$$

where A and B are the stiffness- and mass matrices in d spatial dimensions, $\kappa = 3/2\Delta t$ is a time discretization parameter, and ε is the diffusivity coefficient. Further, let G and $D = G^{\mathrm{T}}$ denote the discrete gradient and divergence operators, respectively. Appropriate boundary conditions are included in these discrete operators. This gives the discrete equations

$$H_\alpha T^{n+1} = B f_T(\mathbf{u}^n, T^n, \mathbf{u}^{n-1}, T^{n-1}, \ldots) \tag{6a}$$

$$H_\nu \mathbf{u}^{n+1} - G p^{n+1} = B f_{\mathbf{u}}(\mathbf{u}^n, \mathbf{u}^{n-1}, \ldots, T^{n+1}) \tag{6b}$$

$$-D\mathbf{u}^{n+1} = 0 \tag{6c}$$

Note that the change of sign in the pressure gradient term in (6b) is caused by an integration by parts in the construction of the weak form of the problem. The temperature equation is, as we noted above, essentially de-coupled from the momentum equation and can hence be solved separately. The remaining dependent variables, velocities and pressure, are computed efficiently by a second-order accurate pressure correction method [21, 22]. If we let Q denote an approximate inverse to the Helmholtz operator, given by a scaled inverse of the diagonal mass matrix, the pressure correction method can be written [23, 24]

$$H\mathbf{u}^* = B\mathbf{f} + G p^n \tag{7a}$$

$$DQG(p^{n+1} - p^n) = -D\mathbf{u}^* \tag{7b}$$

$$\mathbf{u}^{n+1} = \mathbf{u}^* + QG(p^{n+1} - p^n) \tag{7c}$$

where $\mathbf{u}^*$ is an auxiliary velocity field that not necessarily satisfies the continuity equation, i.e. $D\mathbf{u}^* \neq 0$.

The discrete Helmholtz operator is symmetric and diagonally dominant, since the mass matrix of the Legendre discretization is diagonal, and can be efficiently solved by the conjugate gradient method with a diagonal (Jacobi) preconditioner. Whereas the pressure operator DQG is easily computed; it is ill-conditioned. The pressure system is solved by the preconditioned conjugate gradient method, with a multilevel overlapping Schwarz preconditioner based on linear finite elements [25].

3. VERIFICATION OF THE NAVIER–STOKES SOLVER

In this section we present a verification of the Navier–Stokes solver in an isothermal case. As the test problem we use the *Taylor vortices* [26], an exact analytical solution of the two-dimensional Navier–Stokes equations in which all variables have non-trivial solutions:

$$\begin{aligned} u(x,y,t) &= -\cos(\pi x)\sin(\pi y)\mathrm{e}^{-2\pi^2 \nu t} \\ v(x,y,t) &= \sin(\pi x)\cos(\pi y)\mathrm{e}^{-2\pi^2 \nu t} \\ p(x,y,t) &= -\tfrac{1}{4}[\cos(2\pi x)+\cos(2\pi y)]\mathrm{e}^{-4\pi^2 \nu t} \end{aligned} \tag{8}$$

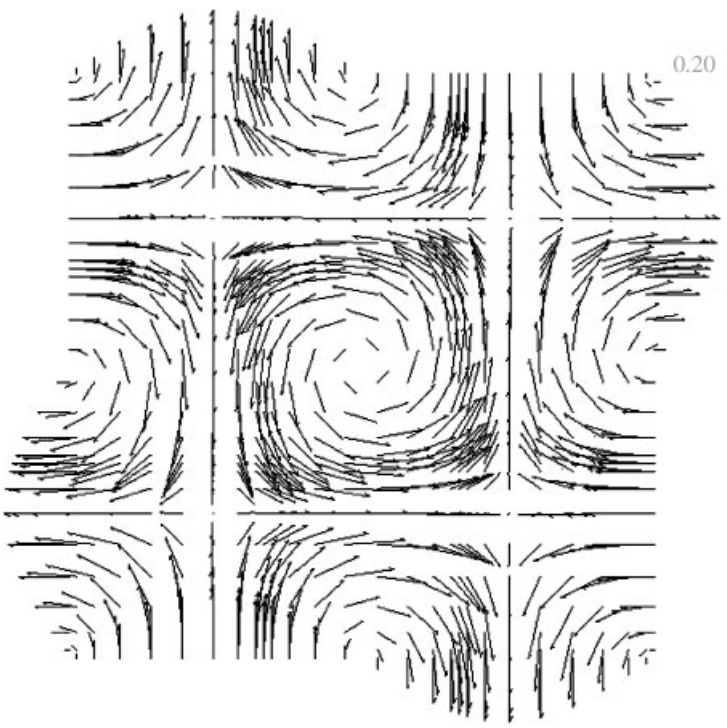

Figure 1. Velocity field for the Taylor vortices (8).

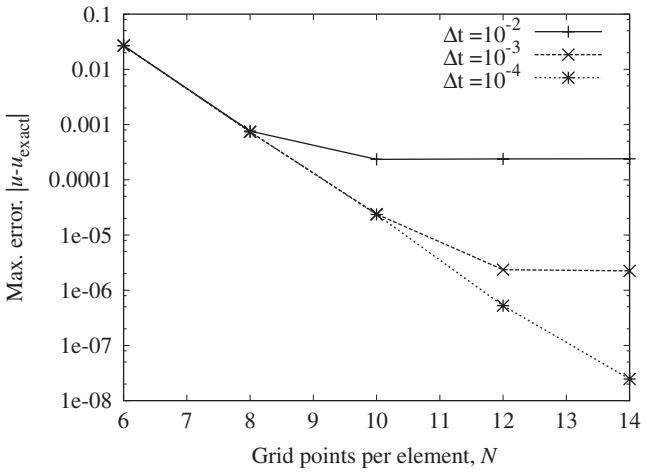

Figure 2. Grid convergence (p-refinement) in u for the Taylor vortices (8). Solutions computed with $M = 2 \times 2$ elements.

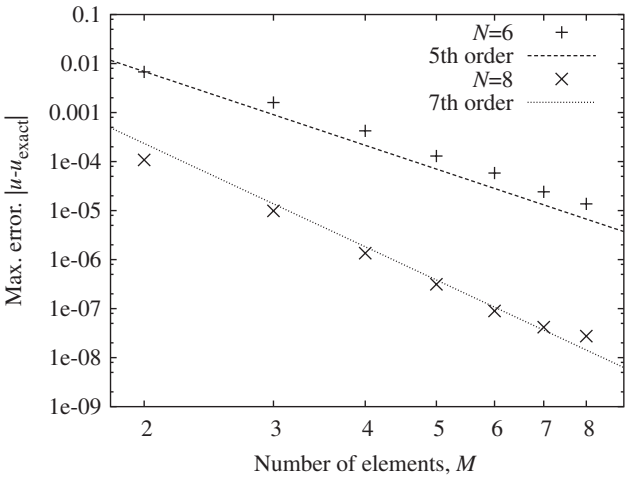

Figure 3. Grid convergence (h-refinement) in u for the Taylor vortices (8). Solutions computed with $N \times N$ grid points in each element.

Although this example is artificially constructed, such that the pressure gradient balances the convective terms and the unsteady terms balance the diffusion, it is useful because both spatial and temporal accuracy in all variables can be checked simultaneously. The exact velocity field is used as initial condition, and the boundary conditions are either periodic, or time-dependent Dirichlet conditions. The velocity field at $t = 0.2$ is shown in Figure 1.

We performed grid convergence studies by independently increasing the number of grid points, N, per element (p-refinement) and the number of elements, M (h-refinement). Figure 2 shows the grid convergence results for p-refinement. As expected, we observe exponential

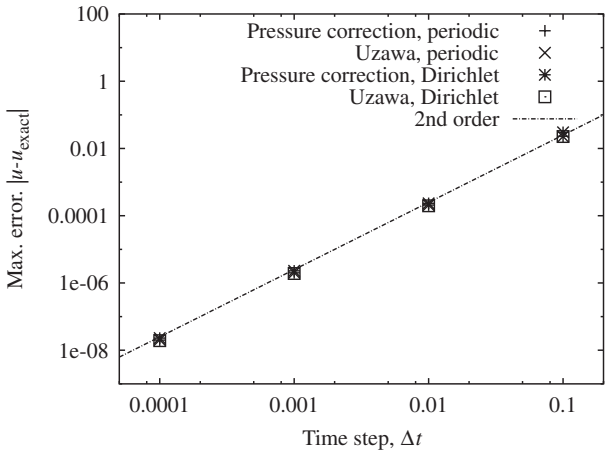

Figure 4. Δt-convergence for the Taylor vortices (8). Computed solutions at $t = 0.2$ with $M = 4 \times 4$ elements and $N = 12 \times 12$ points in each element.

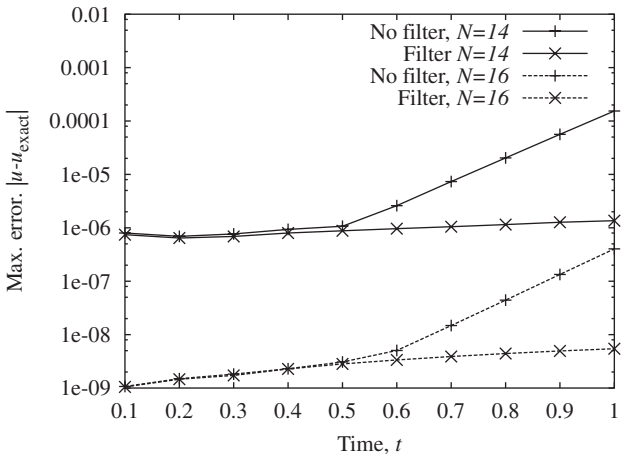

Figure 5. Effect of filtering on error growth, dependence on N. $M = 3 \times 3$, $\nu = 10^{-3}$, $\eta = 0.05$.

convergence when N increases to the point where time-integration errors dominate. Furthermore, we show in Figure 3 that we obtain algebraic convergence for h-refinement (i.e. constant N and increasing M). Hence, for a fixed N the spectral element method converges similarly to a finite-element method of order $(N - 1)$.

We then consider the time accuracy of the computed solutions. The time integration method includes two operator splitting methods; the OIF splitting of advective and diffusive terms and the pressure correction method to compute the velocity and pressure. We performed computations in which we only employed the OIF splitting and solved the velocity–pressure coupling by an exact block LU-decomposition of the discretized Stokes problem known as the Uzawa method, and computations in which we used both splittings. In both cases

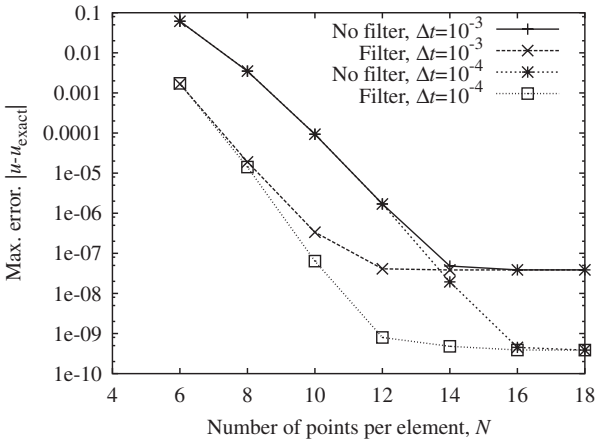

Figure 6. Effect of filtering on the grid convergence (p-refinement) for the Taylor vortices (8). Computed solutions at $t = 0.2$, $M = 3 \times 3$, $v = 10^{-3}$, $\eta = 0.5$.

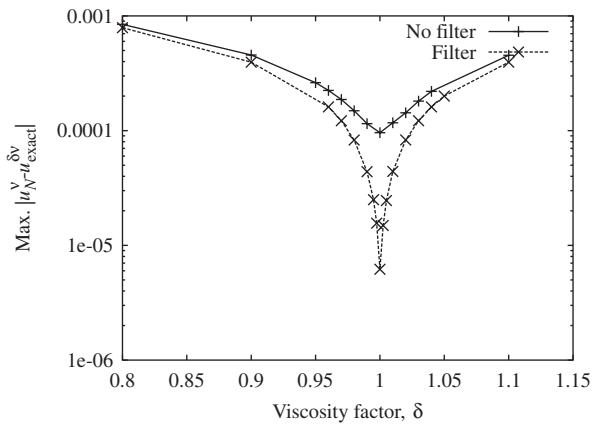

Figure 7. Maximum of $u_N^v - u_{\text{exact}}^{\delta v}$ for the Taylor vortices (8), as function of δ, with and without filtering with $\eta = 0.05$. 3×3 elements, 10×10 grid points in each element.

the method is indeed second-order accurate in the implicit time step, Δt, as we show in Figure 4.

Finally, we investigate the effect of employing the filter, given by Equation (5), proposed by Fischer and Mullen [13]. We compare the time evolution of the errors for filtered and unfiltered simulations, respectively. In the filtered computations, the filter parameter was set to $\eta = 0.05$. In Figure 5, we can observe that exponential error growth sets in after a certain time, and that application of the filter eliminates this spurious error growth.

The spatial convergence of the filtered calculations is depicted in Figure 6, where exponential convergence is observed in both the filtered and non-filtered case. When the accuracy is limited by the spatial resolution, the errors are however several orders of magnitude smaller when filtering is employed.

To establish whether the additional dissipation induced by the filtering actually has the same effect as increasing the viscosity v, thus lowering the effective Reynolds number, we compared the computed solution against the exact solutions based on a scaled viscosity δv where δ is a scaling factor close to unity. The results are shown in Figure 7, and shows that the method with filtering does indeed solve the equations at the correct Reynolds number, and moreover that it performs significantly better than the non-filtered method.

We have also performed a similar verification of the three-dimensional implementation against a Beltrami flow, given in Reference [27], that also have non-trivial solutions in all variables.

4. CAVITY SIMULATIONS

We have performed simulation of the free convection in two-dimensional square and rectangular cavities. The problem comprises a box of side lengths L_x and L_y filled with a Boussinesq fluid characterized by a Prandtl number, $Pr = 0.71$. The vertical walls are kept at constant temperature T_{hot} and T_{cold}, respectively, while the horizontal lid and bottom are insulated with zero heat flux. The direction of gravity is downward, parallel to the heated walls. The cavity flow exhibits a centro-symmetric property [28] in that, for the steady-state base flows, the velocity and temperature fields are skew-symmetric with respect to the diagonal of the cavity, whereas the unstable eigenmodes either share this skew-symmetry or have the opposite symmetry.

The most common diagnostic connected to the free convection cavity flow is the average Nusselt number, which expresses the non-dimensional heat flux across the cavity. The Nusselt number is usually calculated at a vertical line, typically the hot or the cold wall, or as a global average over the entire cavity. The Nusselt number is given by

$$Nu = \frac{Q}{Q_0} \tag{9a}$$

where Q is the computed heat flux through the cavity

$$Q = \int_0^{L_y} \left(uT - \alpha \frac{\partial T}{\partial x} \right) \mathrm{d}y \quad \text{or} \quad Q = \int_0^{L_x} \int_0^{L_y} \left(uT - \alpha \frac{\partial T}{\partial x} \right) \mathrm{d}x \, \mathrm{d}y \tag{9b}$$

for line and volume averages, respectively. The reference value, Q_0, is the corresponding heat flux if the heat transfer were by pure conduction

$$Q_0 = L_y \frac{\alpha \Delta T}{L_x} \quad \text{or} \quad Q_0 = L_x L_y \frac{\alpha \Delta T}{L_x} = L_y \alpha \Delta T \tag{9c}$$

4.1. Square cavity simulations

The steady-state differentially heated square cavity flow was the subject of one of the first benchmark comparison exercises, reported in Reference [29]. The reference results produced in that exercise are given by de Vahl Davis [1]. The results of de Vahl Davis were produced, for Rayleigh numbers in the range 10^3–10^6, using a stream-function/vorticity formulation discretized by a second-order finite difference method on a regular mesh. Later, more accurate

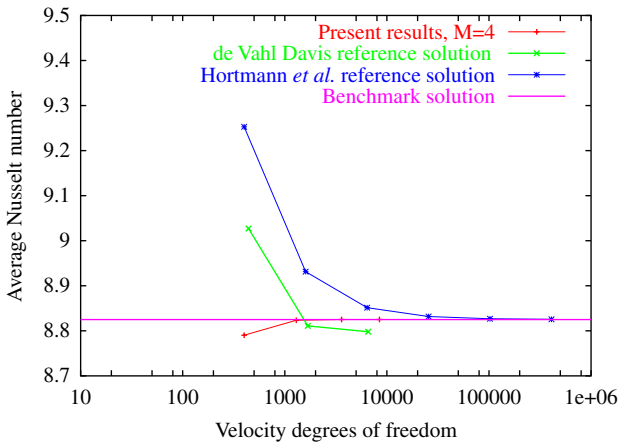

Figure 8. Grid convergence for the average Nusselt number for the square cavity simulation at $Ra = 10^6$.

results obtained by a second-order finite volume method on higher-resolution non-uniform grids were reported by Hortmann *et al.* [2]. Le Quéré [3] used a high-order pseudo-spectral Chebyshev method to extend the benchmark to larger Rayleigh numbers.

As noted in the Introduction, Minev *et al.* [11] reported computational examples of thermal cavity flows obtained by a spectral element method. In that work only the Nusselt numbers were reported, and the heat flux at the wall was computed by first-order finite differences. Furthermore, they did not refine the mesh sufficiently to converge the simulations to a steady state at the highest Rayleigh number. Below we present a comprehensive comparison against several parameters from available reference solutions. We used spectral calculations to compute the derived quantities. All calculations were started from rest, and converged to steady state through time marching. We performed grid refinement to verify the convergence of the diagnostic quantities.

For the lower Rayleigh numbers, we performed simulations using $M = 4 \times 4$ elements varying the resolution in each element from $N = 6 \times 6$ to 24×24. In Figure 8 we show the grid convergence of the computed global Nusselt numbers for $Ra = 10^6$ compared to the previously reported benchmark results [1–3]. Note the excellent agreement with the reference data; even the coarsest resolution (i.e. 21×21 grid points) produces a solution within 0.5% of the reference data. For the smaller Rayleigh number, all computations are essentially converged. In Table I we compare the Nusselt numbers obtained at the finest grid with the 'grid-independent' values from the reference solutions obtained by Richardson extrapolation or by grid convergence.

For the higher Rayleigh numbers we performed a detailed comparison of several diagnostic quantities against the reference solution from Reference [3]. The comparison comprised the following quantities:

- The value of the streamfunction in the centre of the cavity, ψ_{mid}, as well as the magnitude and location of the streamfunction maxima in the upper left quadrant, ψ_1 and ψ_2.

Table I. Computed Nusselt numbers for the square cavity compared to the reference solutions of de Vahl Davis (dVD) [1], Hortmann *et al.* (HPS) [2], and Le Quéré (LQ) [3].

	$\overline{Nu}$			$Nu_{\max}$		
Ra	10^4	10^5	10^6	10^4	10^5	10^6
Present results	2.245	4.522	8.825	3.531	7.720	17.539
de Vahl Davis	2.243	4.519	8.800	3.528	7.717	17.925
Hortmann *et al.*	2.245	4.522	8.825	3.531	7.720	17.536
Le Quéré	—	—	8.825	—	—	17.536

dVD: stream function/vorticity formulation, second-order finite difference discretization, uniform grid, Richardson extrapolation.
HPS: primitive variable formulation, finite volume discretization, non-uniform grid, Richardson extrapolation.
LQ: primitive variables, pseudo-spectral Chebyshev discretization, mesh converged solution.

- The magnitude and location of the maximum u-velocity along the vertical centreline of the cavity, $u_{\mathrm{cl,max}}$, and correspondingly the maximum v-velocity along the horizontal centreline, $v_{\mathrm{cl,max}}$.
- The mean Nusselt number at the hot wall, Nu_0, and at the centreline, $Nu_{1/2}$. Moreover, the maximum and minimum local Nusselt numbers at the hot wall, with their corresponding locations.

We computed the average Nusselt numbers by spectral differentiation of the temperature field and GLL quadrature. Furthermore, the stream function was computed by a spectral element solution of the Poisson equation

$$\nabla^2\psi = -(v_x - u_y), \quad \psi|_{\partial\Omega} = 0$$

where u and v are the components of the converged steady-state velocity field. To determine maxima and minima in the solution, we followed the same procedure as Le Quéré [3], interpolating spectrally from the GLL mesh to a uniform 1000×1000 grid covering the cavity. The results are summarized in Tables II–IV. The present results correspond very well with the reference data; most quantities converge to the benchmark results within at least four significant digits. Note, however, the larger discrepancies in the wall Nusselt numbers. The wall quantities appear to converge slower to the reference than the other quantities, indicating that the large gradients in the boundary layers are not properly resolved. The mean wall Nusselt number is nevertheless within half a per cent of the reference value at the largest Rayleigh number, whereas the difference for the maximum Nusselt number is somewhat larger. Finally, we note that all the computed maxima and minima correspond well with the reference solution both with respect to magnitude and to position.

Le Quéré and Behnia [30] showed that the critical Rayleigh number for transition from steady state to time-dependent flow in the square cavity is $Ra = (1.82 \pm 0.01) \times 10^8$. To investigate the behaviour of the present spectral element method close to the transition, we performed long time simulations for slightly sub- and super-critical Rayleigh numbers; *viz.* $Ra = 1.80 \times 10^8$ and $Ra = 1.85 \times 10^8$, respectively. In both cases we used $M = 12 \times 12$ elements

Table II. Computed diagnostic quantities for the square cavity at $Ra = 10^6$ compared to the reference solutions of Le Quéré (LQ) [3].

Run	M4N10	M4N14	M4N18	M6N6	M6N10	M6N14	LQ
# points	37×37	53×53	71×71	31×31	55×55	79×79	
$10^3\lvert\psi_{\text{mid}}\rvert$	16.373	16.385	16.384	16.519	16.378	16.384	16.386
$10^3\lvert\psi_1\rvert$	16.796	16.810	16.809	16.931	16.803	16.809	16.811
x	0.151	0.150	0.150	0.152	0.150	0.150	0.150
y	0.547	0.543	0.547	0.554	0.547	0.547	0.547
$u_{\text{cl, max}}$	0.06487	0.06484	0.06485	0.06514	0.06488	0.06485	0.06483
y	0.850	0.850	0.850	0.845	0.850	0.850	0.850
$v_{\text{cl, max}}$	0.2204	0.2206	0.2206	0.2214	0.2204	0.2205	0.2206
x	0.038	0.038	0.038	0.039	0.038	0.038	0.038
$\overline{Nu}$	8.822	8.825	8.825	8.878	8.824	8.825	
Nu_0	8.700	8.837	8.824	8.486	8.840	8.824	8.825
$Nu_{1/2}$	8.823	8.825	8.825	8.782	8.825	8.825	8.825
$Nu_{\max}$	16.388	17.659	17.524	20.502	17.438	17.539	17.536
y	0.035	0.040	0.039	0.037	0.043	0.039	0.039
$Nu_{\min}$	0.9772	0.9794	0.9795	1.0090	0.9794	0.9796	0.9795
y	1.0	1.0	1.0	0.999	0.999	0.999	1.0

LQ: primitive variables, pseudo-spectral Chebyshev discretization, mesh converged solution.

Table III. Computed diagnostic quantities for the square cavity at $Ra = 10^7$ compared to the reference solutions of Le Quéré (LQ) [3].

Run	M4N10	M4N14	M4N18	M6N6	M6N10	M6N14	LQ
# points	37×37	53×53	71×71	31×31	55×55	79×79	
$10^3\lvert\psi_{\text{mid}}\rvert$	9.309	9.282	9.284	10.335	9.275	9.284	9.285
$10^3\lvert\psi_1\rvert$	9.603	9.533	9.538	11.778	9.518	9.538	9.539
x	0.084	0.086	0.086	0.083	0.086	0.086	0.086
y	0.559	0.555	0.556	0.524	0.557	0.556	0.556
$10^3\lvert\psi_2\rvert$	8.330	8.410	8.413	10.540	8.411	8.413	8.413
x	0.119	0.125	0.125	0.111	0.126	0.125	0.125
y	0.877	0.875	0.875	0.870	0.876	0.875	0.875
$u_{\text{cl, max}}$	0.04699	0.04699	0.04699	0.04987	0.04697	0.04699	0.04699
y	0.881	0.879	0.879	0.888	0.880	0.879	0.879
$v_{\text{cl, max}}$	0.2155	0.2208	0.2211	0.2330	0.2206	0.2211	0.2211
x	0.021	0.021	0.021	0.029	0.021	0.021	0.021
$\overline{Nu}$	16.423	16.520	16.523	15.954	16.511	16.523	
Nu_0	15.321	16.372	16.557	19.199	15.912	16.553	16.523
$Nu_{1/2}$	16.428	16.520	16.523	15.926	16.512	16.523	16.523
$Nu_{\max}$	45.35	36.05	39.49	49.03	37.65	38.94	39.39
y	0.016	0.015	0.020	0.051	0.011	0.020	0.018
$Nu_{\min}$	1.403	1.365	1.366	1.452	1.366	1.366	1.366
y	1.0	1.0	1.0	0.999	0.999	0.999	1.0

LQ: primitive variables, pseudo-spectral Chebyshev discretization, mesh converged solution.

Table IV. Computed diagnostic quantities for the square cavity at $Ra = 10^8$ compared to the reference solutions of Le Quéré (LQ) [3].

Run	M6N14	M6N18	M8N14	M8N18	M12N10	M12N12	LQ
# points	79×79	103×103	71×71	137×137	111×111	133×133	
$10^3\lvert\psi_{\text{mid}}\rvert$	5.226	5.232	5.231	5.232	5.228	5.232	5.232
$10^3\lvert\psi_1\rvert$	5.379	5.385	5.383	5.385	5.380	5.384	5.385
x	0.048	0.048	0.048	0.048	0.048	0.048	0.048
y	0.553	0.553	0.553	0.553	0.553	0.553	0.553
$10^3\lvert\psi_2\rvert$	4.477	4.485	4.483	4.482	4.484	4.482	4.482
x	0.101	0.102	0.102	0.102	0.101	0.102	0.102
y	0.896	0.895	0.895	0.895	0.896	0.895	0.895
$u_{\text{cl, max}}$	0.03220	0.03216	0.03218	0.03219	0.03214	0.03218	0.03219
y	0.928	0.928	0.928	0.928	0.928	0.928	0.928
$v_{\text{cl, max}}$	0.2222	0.2222	0.2220	0.2222	0.2221	0.2220	0.2222
x	0.012	0.012	0.012	0.012	0.012	0.012	0.012
$\overline{Nu}$	30.212	30.224	30.221	30.225	30.214	30.223	
Nu_0	29.426	30.225	30.017	30.259	29.424	30.094	30.225
$Nu_{1/2}$	30.213	30.224	30.221	30.225	30.221	30.223	30.225
$Nu_{\max}$	83.42	81.96	79.36	86.70	85.43	80.30	87.24
y	0.005	0.009	0.006	0.009	0.006	0.007	0.008
$Nu_{\min}$	1.917	1.922	1.919	1.919	1.917	1.919	1.919
y	0.999	0.999	1.0	1.0	1.0	1.0	1.0

LQ: primitive variables, pseudo-spectral Chebyshev discretization, mesh converged solution.

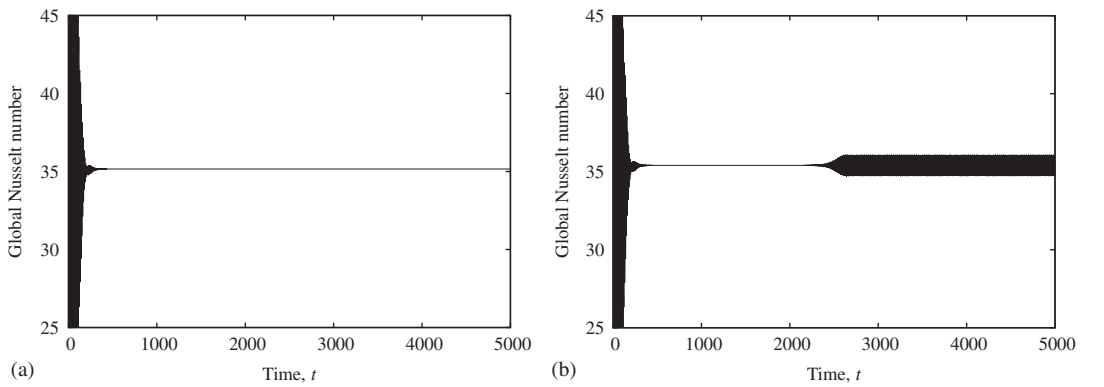

Figure 9. Time histories of the global Nusselt number for convection in the square cavity close to the critical Rayleigh number: (a) sub-critical, $Ra = 1.80 \times 10^8$; and (b) super-critical, $Ra = 1.85 \times 10^8$.

with $N = 12 \times 12$ grid points in each, i.e. 133×133 grid points in total, and we used the same time step as for the steady-state simulation at $Ra = 10^8$ corresponding to $\Delta t \approx 8 \times 10^{-3}$ in convective time units. Both simulations were started from rest and run for long enough to ensure that we reach the time asymptotic state. We show time histories for the global Nusselt number in Figure 9. The sub-critical simulation at $Ra = 1.80 \times 10^8$ reached a steady state

after about 500 convective time units, and the simulation was then continued until 14 000 time units without any time-dependent modes appearing in the solution. In the slightly supercritical simulation at $Ra = 1.85 \times 10^8$, we also observe that the initial transient is damped out to what appears to be a steady state. In this case, however, we observe that a time-dependent mode grows to establish an oscillatory asymptotic solution after approx. 3000 convective time units. We can therefore conclude that the present spectral element method can predict the critical Nusselt number at least to within about 1% by straightforward computations starting from rest.

4.2. Tall cavity simulations

Christon *et al.* [4] summarize the results of a workshop discussing the free convection in a tall cavity with aspect ratio 8:1. The comparison was performed for a Rayleigh number, $Ra = 3.4 \times 10^5$, that is slightly above the transition point from steady state to time-dependent flow at $Ra \approx 3.1 \times 10^5$. A total of 31 solutions were submitted to the workshop, of these a pseudo-spectral solution, contributed by Xin and Le Quéré [5] using a spatial resolution of 48×180 modes was selected as the reference solution.

In addition to the wall and centreline Nusselt number (9), we will employ several global and point measures of the solution for the comparison with the benchmark. The global velocity metric is related to the total kinetic energy and is given by

$$U = \sqrt{\frac{1}{2L_xL_y}\int_0^{L_x}\int_0^{L_y} \mathbf{u}\cdot\mathbf{u}\,\mathrm{d}x\,\mathrm{d}y} \tag{10}$$

while the vorticity metric is

$$\Omega = \sqrt{\frac{1}{2L_xL_y}\int_0^{L_x}\int_0^{L_y} (v_x - u_y)^2\,\mathrm{d}x\,\mathrm{d}y} \tag{11}$$

We computed all the above integral measures by spectral differentiation, where applicable, and GLL quadrature. Furthermore point values for non-dimensional temperature, θ, velocity components, u and v, vorticity, ω, and stream function, ψ, were monitored at the location ($x_1 = 0.181 \times L_x,\ y_1 = 7.37 \times L_x$). The vorticity was computed by spectral differentiation, whereas the stream function was computed as the volume flux across a line connecting the cavity wall and the monitor location. To determine this flux, the velocity components were interpolated spectrally to the integration contour and the line integral was determined by Simpson quadrature. We have confirmed that we use enough sampling points along the integration contour such that the reported values of the stream function are converged. Furthermore, the skew-symmetry of the solution was monitored by the skewness metric

$$\varepsilon_{12} = \theta(x_1, y_1) + \theta(x_2, y_2) \tag{12}$$

where $x_2 = L_x - x_1$ and $y_2 = L_y - y_1$. Finally, we monitored pressure differences in the flow; across the top of the cavity and in the boundary layer along the hot wall. We employed spectral interpolation, using the GLL Lagrange interpolant functions, to compute the function values at the monitor locations. For each diagnostic variable we computed the mean value and peak-to-valley oscillation amplitudes by averaging over several periods after the flow reached a statistically steady state.

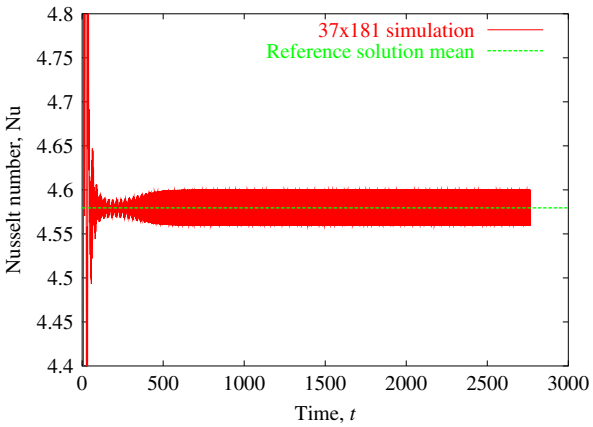

Figure 10. Time evolution of the global Nusselt number for the tall cavity simulation at $Ra = 3.4 \times 10^5$.

The computed results depend on the governing equations, the boundary conditions, and the spatial and temporal resolution given by the grid size and time step. Furthermore, several algorithmic parameters—such as the weight factor in the filter given by Equation (5) and different tolerance parameters related to the iterative solvers and the adaptive time integration of the advective terms—influence the solution. We have investigated the sensitivity of the diagnostic variables to variations in several of these parameters, *viz*

- Grid size. We used a uniform $M = 4 \times 20$ element grid in all simulations, varying the number of points per element from $N = 6 \times 6$ up to $N = 18 \times 18$. The coarsest grid we employed thus comprised 21×101 velocity grid points, whereas the finest grid had 69×341 points.
- Time step, Δt.
- Tolerance parameter for the solution of the velocity and temperature Helmholtz problems, `htol`.
- Tolerance parameter for the solution of the pressure equation, `ptol`.
- Filter parameter, η.

For most of the simulations we performed, the implicit time steps were so short that the results are essentially converged in time. Furthermore, the errors in the explicit integration of the advective terms are much smaller than any meaningful choice of the integration tolerance `atol`. We have therefore not considered the impact of this parameter on the computed solutions.

4.2.1. Baseline solution. For the baseline solution we consider a series of simulations performed with the tolerance parameters for the Helmholtz and pressure solvers were both set to strict values $\texttt{htol} = \texttt{ptol} = 10^{-9}$. We used a regular element grid with $M = 4 \times 20$ elements, and performed spatial and temporal refinement by varying the number of points per element, N, and time step, Δt, respectively.

In Figure 10, we show a typical time history for the global Nusselt number; after the initial transient the flow reaches a statistically steady oscillatory state after about 1000 buoyancy

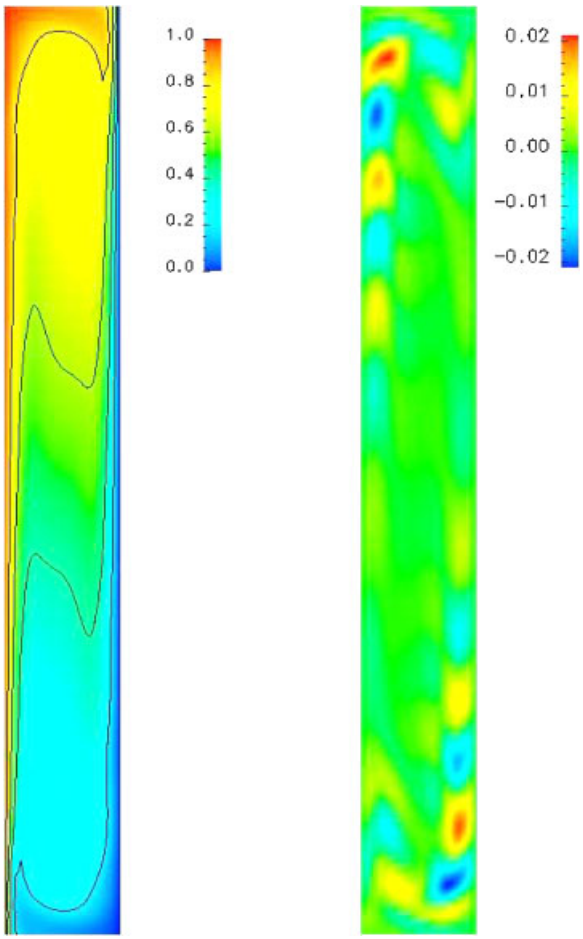

Figure 11. Computed instantaneous and fluctuating temperature field for the tall cavity simulation at $Ra = 3.4 \times 10^5$.

time units, $\tau_0 = \sqrt{Pr/(v^2 Ra)}$. Note, however, that several other measures require significantly longer times to converge. In particular the time history for the skewness metric attains its asymptotic state after approx. 2500 time units. Furthermore, Figure 11 shows the instantaneous and fluctuating temperature fields for the final state. Note the skew-symmetry of the solution, the shape and sign of the travelling wave structures are mirrored about the diagonal of the cavity.

We display the spatial convergence for the Wall Nusselt number, Nu_0, in Figure 12. Furthermore, we show the time history for the oscillation of the vertical velocity component in the monitor point, $v_1 = v(x_1, y_1)$ in Figure 13. In general, both integral and point measures are close to their converged values already at the second coarsest grid, i.e. for $N = 10 \times 10$. The only exception is the mean of the pressure differences—Δp_{14}, Δp_{35}, and Δp_{51}—which we discuss below.

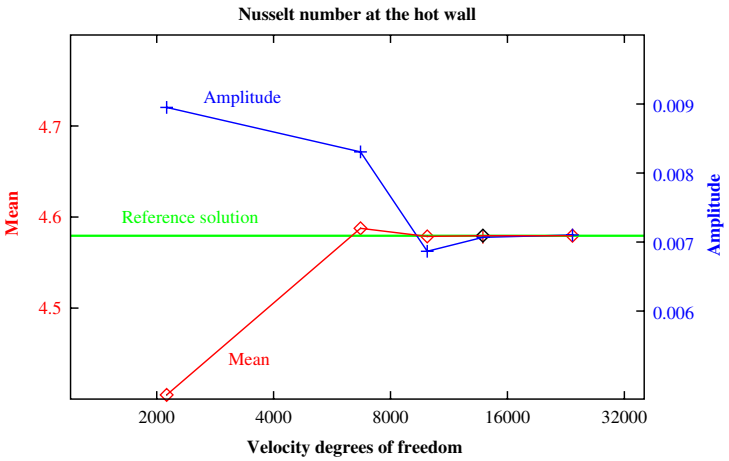

Figure 12. Grid convergence for the mean and oscillations amplitude of the hot wall Nusselt number for the tall cavity simulation at $Ra = 3.4 \times 10^5$.

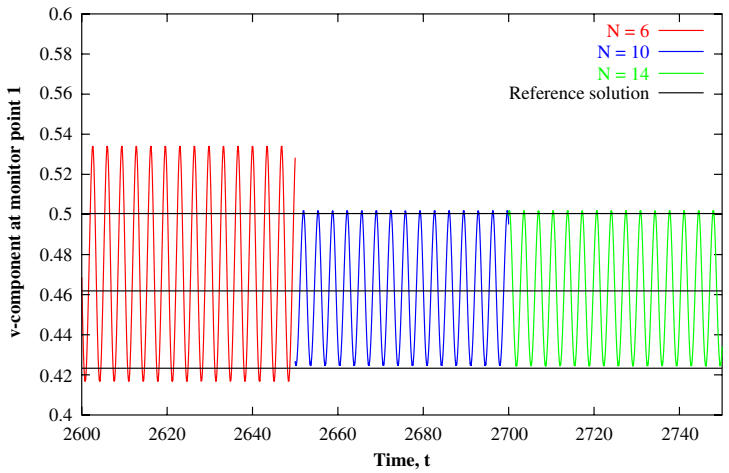

Figure 13. Oscillations of the point vertical velocity, v_1, for the tall cavity simulation at $Ra = 3.4 \times 10^5$.

Several of the integral and point measures are fairly well approximated even for the coarsest resolution. We see little dependence on the time step in the computed results; this indicates that the temporal resolution is sufficient. Note, however, that we could only use the largest time step on the two coarsest grids because of CFL-like restrictions in the explicit integration of the advective terms.

4.2.2. Convergence of pressure differences. The benchmark includes data for three pressure differences, one across the top of the cavity, denoted Δp_{14}, and two in the boundary layer along

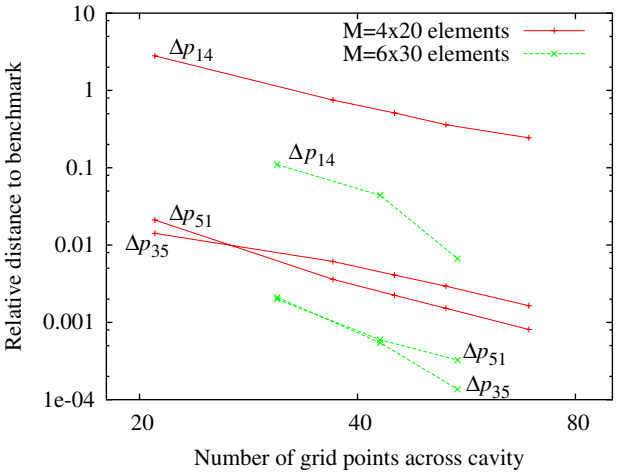

Figure 14. Relative error, measured as the distance to the benchmark data, for the monitored pressure differences in the tall cavity.

the hot wall, denoted Δp_{35} and Δp_{51}. The spectral element discretization is discontinuous across element interfaces. We can therefore not expect that the method computes reasonable pressure differences across elements.

Note, however, that the pressure differences computed by the method does indeed converge, algebraically in the number of grid points, to the reference data as shown in Figure 14. The convergence of the pressure differences can be explained from the application of the overlapping preconditioner for the pressure operator. This preconditioner is the operator that is actually inverted in the iterations for the pressure solution. It is based on linear finite elements and provides a coupling of the pressure levels in adjacent elements through the overlap region.

4.2.3. Dependence on tolerance parameters. We performed a series of simulations in which we varied the numerical tolerance parameters for the iterative solution of the Helmholtz problems for the velocities and temperature, and the pressure operator. We see little dependence on pressure tolerance in the computed results. This is fortunate because the poor conditioning of the pressure operator DQG in (7) means that sharpening the pressure tolerance can lead to a significant increase in the number of iterations needed to converge, and hence in the CPU time required to compute the solution. There is, on the other hand, a definite dependence on the Helmholtz tolerance. In this case, sharpening the tolerance clearly leads to improved solution quality, and this improvement is obtained at reasonable cost as the Helmholtz operators are diagonally dominant and thus converge rapidly. Based on these experiments, we arrive at a set of *practical* settings for the tolerance parameters, $\texttt{htol} = 10^{-9}$ and $\texttt{ptol} = 10^{-6}$, as a reasonable compromise between solution accuracy and efficiency. With these settings both the predicted means and oscillation amplitudes differ from the strict tolerance solution by less than 1% for all quantities.

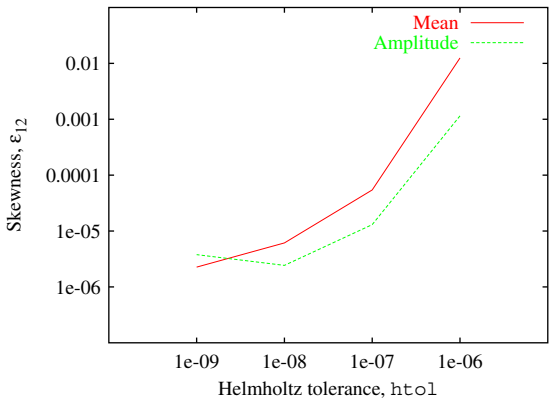

Figure 15. Dependence of the skewness metric, ε_{12} on the Helmholtz tolerance parameter, `htol`, $N = 14$ simulation.

4.2.4. The skewness metric. Because of the centro-symmetric property of the base flow, the skewness metric ε_{12} defined in (12) will, in principle, be identically zero for unstable modes that preserve the skew-symmetry. Xin and Le Quéré [5] showed that only one unstable mode exists at the Rayleigh number considered by the benchmark, $Ra = 3.4 \times 10^5$, and this mode is skew-symmetry preserving.

In all our simulations, the skew-symmetry metric, ε_{12}, oscillates with small mean and amplitude. Two factors appear to contribute to the magnitude of the oscillations. Firstly, and most importantly, the oscillation mean and amplitude depend directly on the Helmholtz tolerance as we show in Figure 15. Reducing `htol` leads to a decrease in ε_{12}. Secondly, the monitor locations do not coincide with the grid points. The solution must therefore be interpolated, and we can detect a small influence of the interpolation errors on ε_{12}. We therefore conclude that ε_{12} is zero within the accuracy of the numerical method, and hence that the computed solutions do indeed preserve the skew-symmetry of the base flow.

4.2.5. Impact of filtering. We can clearly see the importance of controlling the aliasing errors in Figure 16 in which we show the evolution of the velocity metric during the initial transient. For these simulations we used $M = 4 \times 20$ and $N = 10$ which, we have seen above, is sufficient to converge most quantities of interest, in particular the integral measures such as the Nusselt number. If we perform this simulation with no filtering, the kinetic energy blows up early in the transient whereas a small amount of filtering is sufficient to suppress the error growth and to stabilize the simulation. To demonstrate that the filtering does not impact the computed solutions much, we show in Figure 17 that there is no visible dependence on the value of the filter parameter for the oscillations of point values, represented by the temperature. We do, however, observe a slight increase in the kinetic energy norm with increasing η.

4.2.6. Finally: the benchmark results. Based on the discussion above we present our best shot at the solution, in Table V. We use the results from the baseline simulation with $M = 4 \times 20$ elements, $N = 18 \times 18$ points per element, $\Delta t = 3.46 \times 10^{-3}$ buoyancy time units, and the filter parameter $\eta = 0.5$ to produce the table. The computed mean values and oscillation amplitudes

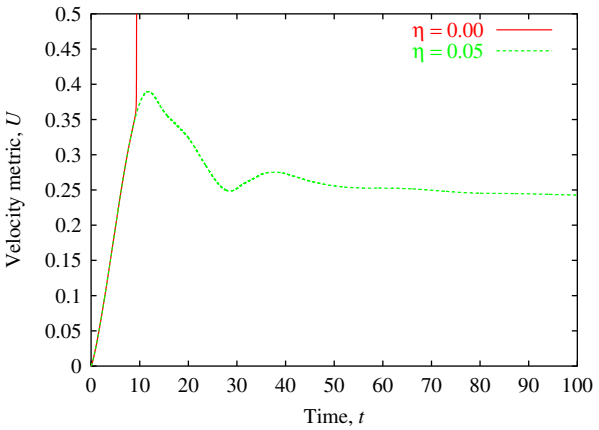

Figure 16. Effect of filtering on the time history of the velocity metric, U, during the initial transient.

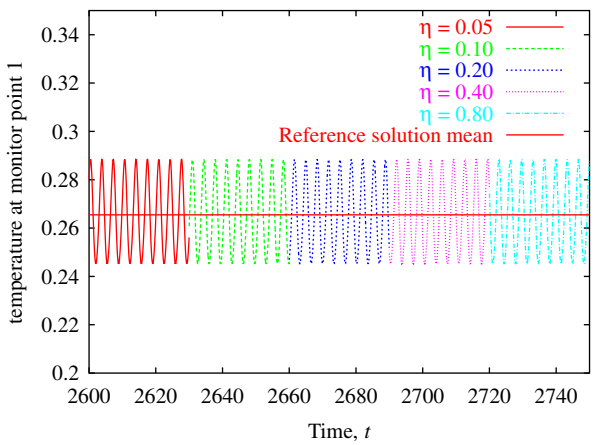

Figure 17. Time history of the point temperature for different filter parameters, η, when the flow is in the statistically steady state.

are denoted by an overbar and a prime, respectively, in the table. The data are compared to the accurate reference solution of Xin and Le Quéré [5]. Note, however, that not all the quantities we consider are available in Reference [5]. For these quantities we compare, in Table VI, the present results with the mean and scatter, given by the standard deviation σ, of the solutions summarized in Reference [4]. For most quantities, the present solution corresponds very well with the reference data with differences significantly less than 1%. There are some exceptions though; for derived quantities such as the stream function and vorticity we observe larger deviations. The mean values of these quantities are nevertheless well within the scatter of the available solutions.

Table V. Computed diagnostic quantities for the simulation of a tall cavity at $Ra = 3.4 \times 10^5$ compared with the reference solution of Xin and Le Quéré [5].

	$\overline{Nu_0}$	Nu'_0	$\overline{Nu_{cl}}$	Nu'_{cl}
Present results	4.57933	7.1026e-2	4.57947	0.17790
Reference	4.57946	7.0936e-2	4.57946	0.17761
Difference (%)	0.0007	0.127	0.0002	0.14
	$\overline{u_1}$	u'_1	$\overline{v_1}$	v'_1
Present results	5.6220e-2	5.4880e-2	0.46173	7.7726e-2
Reference	5.6356e-2	5.4828e-2	0.46188	7.7123e-2
Difference (%)	0.228	0.178	0.033	0.149
	$\overline{\theta_1}$	θ'_1	τ_θ	
Present results	0.265612	4.2774e-1	3.4109	
Reference	0.265480	4.2740e-2	3.4115	
Difference (%)	0.050	0.199	0.018	

Table VI. Computed diagnostic quantities for the simulation of a tall cavity at $Ra = 3.4 \times 10^5$ for parameters that were not provided in the reference solution of Xin and Le Quéré [5]. For these quantities the comparison is based on the average and the scatter, σ, of the 29 solutions summarized by Christon *et al.* [4].

	$\overline{U}$	U'	$\overline{\Omega}$	Ω'
Present results	0.2395	3.354e-5	3.0171	3.198e-3
Reference	0.2397	4.093e-5	2.9998	3.488e-3
Difference (%)	0.078	18.05	0.576	8.302
Difference/σ	0.188	0.608	0.223	0.679
	$\overline{\psi_1}$	ψ'_1	$\overline{\omega_1}$	ω'_1
Present results	−7.509e-2	2.493e-3	−2.3678	1.0801
Reference	−7.249e-2	7.864e-3	−2.2845	1.2325
Difference (%)	3.58	68.3	3.65	12.4
Difference/σ	0.76	3.2	0.58	0.50

5. CONCLUDING REMARKS

We have performed a comprehensive assessment of the accuracy of a spectral element method for both steady state and time-dependent free convection in square and rectangular cavities. Both the steady-state solutions, obtained by time marching, and the supercritical time-dependent solutions show excellent agreement with the benchmark references. The demonstrated accuracy combined with the flexibility of spectral element methods, improve our confidence in the method as a tool to explore transitional and turbulent flows.

REFERENCES

1. de Vahl Davis G. Natural convection in a square cavity: a bench mark numerical solution. *International Journal for Numerical Methods in Fluids* 1983; **3**:249–264.

2. Hortmann M, Perić M, Scheurer G. Finite volume multigrid prediction of laminar natural convection: bench-mark solutions. *International Journal for Numerical Methods in Fluids* 1990; **11**:189–207.
3. Le Quéré P. Accurate solutions to the square thermally driven square cavity at high Rayleigh number. *Computers and Fluids* 1991; **20**:29–41.
4. Christon MA, Gresho PM, Sutton SB. Computational predictability of time-dependant natural convection flows in enclosures (including a benchmark solution). *International Journal for Numerical Methods in Fluids* 2002; **40**:953–980.
5. Xin S, Le Quéré P. An extended Chebyshev pseudo-spectral benchmark for the 8:1 differentially heated cavity. *International Journal for Numerical Methods in Fluids* 2002; **40**:981–998.
6. Paul MR, Cross MC, Fischer PF, Greenside HS. Power-law behavior of power spectra in low Prandtl number Rayleigh–Benard convection. *Physical Review Letters* 2001; **8715**(15):154501.
7. Paul MR, Chiam KH, Cross MC, Fischer PF, Greenside HS. Pattern formation and dynamics in Rayleigh–Benard convection: numerical simulations of experimentally realistic geometries. *Physical Review D* 2003; **184**(1–4):114–126.
8. Greiner M, Spencer GJ, Fischer PF. Direct numerical simulation of three-dimensional flow and augmented heat transfer in a grooved channel. *Journal of Heat Transfer—Transactions of the ASME* 1998; **120**(3):717–723.
9. Greiner M, Faulkner RJ, Van VT, Tufo HM, Fischer PF. Simulations of three-dimensional flow and augmented heat transfer in a symmetrically grooved channel. *Journal of Heat Transfer—Transactions of the ASME* 2000; **122**(4):653–660.
10. Greiner M, Fischer PF, Tufo HM, Wirtz RA. Three-dimensional simulations of enhanced heat transfer in a flat passage downstream from a grooved channel. *Journal of Heat Transfer—Transactions of the ASME* 2002; **124**(1):169–176.
11. Minev PD, Van de Vosse FN, Timmermans LJP, Van Stenhoven AA. A second order splitting algorithm for thermally driven flow problems. *International Journal of Numerical Methods for Heat and Fluid Flow* 1995; **6**:51–60.
12. Gunes H. Low-order dynamical models of thermal convection in high-aspect ratio enclosures. *Fluid Dynamics Research* 2002; **30**:1–29.
13. Fischer PF, Mullen JS. Filter-based stabilization of spectral element methods. *Comptes Rendus de l'Académie des sciences Paris*, *t.332*, *Série I—Analyse numérique* 2001; 265–270.
14. Couzy W. Spectral element discretization of the unsteady Navier–Stokes equations and its iterative solution on parallel computers. *Ph.D. Thesis*, École Polytechnique Fédérale de Lausanne, 1995.
15. Fischer PF. An overlapping Schwarz method for spectral element solutions of the incompressible Navier–Stokes equations. *Journal of Computational Physics* 1997; **133**:84–101.
16. Maday Y, Patera A, Rønquist EM. An operator-integration-factor method for time-dependent problems: application to incompressible fluid flow. *Journal of Scientific Computing* 1990; **4**:263–292.
17. Patera AT. A spectral element method for fluid dynamics: laminar flow in a channel expansion. *Journal of Computational Physics* 1984; **54**:468–488.
18. Maday Y, Patera AT. Spectral element methods for the incompressible Navier–Stokes equations. In *State-of-the-Art Surveys on Computational Mechanics*, Chapter 3, Noor AK, Oden JT (eds). ASME: New York, 1989.
19. Fischer PF. Private communication, May 2002.
20. Kirby RM, Karniadakis GE. De-aliasing on non-uniform grids: algorithms and applications. *Journal of Computational Physics* 2003; **191**:249–264.
21. Chorin AJ. Numerical solution of the Navier–Stokes equations. *Mathematics of Computation* 1968; **23**:351–354.
22. Van Kan J. A second-order accurate pressure-correction scheme for viscous incompressible flow. *SIAM Journal on Scientific and Statistical Computing* 1986; **7**:870–891.
23. Blair Perot J. An analysis of the fractional step method. *Journal of Computational Physics* 1993; **108**:51–58.
24. Couzy W. Spectral element discretization of the unsteady Navier–Stokes equations and its iterative solution on parallel computers. *Ph.D. Thesis*, *Thèse No. 1380*, École Polytechnique Fédérale de Lausanne, 1995.
25. Fischer PF, Miller NI, Tufo HM. An overlapping Schwarz method for spectral element simulation of three-dimensional incompressible flows. In *Parallel Solution of Partial Differential Equations*, Bjørstad P, Luskin M (eds). Springer: Berlin, 2000; 159–180.
26. Taylor GI. On the decay of vortices in a viscous fluid. *Philosophical Magazine* 1923; **46**:671–674.
27. Ethier CR, Steinman DA. Exact fully 3D Navier–Stokes solutions for benchmarking. *International Journal for Numerical Methods in Fluids* 1994; **19**:369–375.
28. Gill AE. The boundary-layer regime for convection in a rectangular cavity. *Journal of Fluid Mechanics* 1966; **26**:515–536.
29. de Vahl Davis G, Jones IP. Natural convection in a square cavity: a comparison exercise. *International Journal for Numerical Methods in Fluids* 1983; **3**:227–248.
30. Le Quéré P, Behnia M. From onset of unsteadiness to chaos in a differentially heated square cavity. *Journal of Fluid Mechanics* 1998; **359**:81–107.

